Investigation on the Performance of Volatile Distributors with Different Configurations under Different Fluidization Regimes

energy&fuels

pubs.acs.org/EF

Article

Investigation on the Performance of Volatile Distributors with Different Configurations under Different Fluidization Regimes

Xiaoyun Li,* Anders Lyngfelt, David Pallarès, Carl Linderholm, and Tobias Mattisson

Cite This: *Energy Fuels* 2022, 36, 9571−9587

Read Online

ACCESS | Metrics & More | Article Recommendations

ABSTRACT: The uniform horizontal distribution of volatiles over the cross section of a fluidized bed with the purpose to obtain good contact between volatiles and bed materials is a key issue to improve the gas conversion in the fuel reactor of chemical looping combustion of solid fuels. The effectiveness of the volatile distributor (VD) concept on the lateral distribution of volatiles in a fluidized bed has been investigated under different operational conditions using a cold-flow model. Furthermore, the performance of the VD has been examined using different configurations of the holes used to distribute the volatiles. The fluidization regimes, i.e., single bubble regime, with only one large bubble formed at a time at the bottom bed, exploding bubble regime, with irregular bubbles containing more particles, and multiple bubble regime, with many small bubbles formed and distributed in the bed, are determined by visual observation of the bottom riser and analysis of the pressure fluctuations, including frequency analysis. The VDs with uneven hole arrangements, which have less distribution holes at the simulated volatile inlet side and a larger open area far from the inlet, provide a more even horizontal distribution of volatiles compared to the VD with equally distributed holes. A larger simulated volatile flow and less open area of the VD increase the pressure drop over the distribution holes and improve the horizontal distribution. In general, the VD gives a more uniform distribution of the volatiles under the exploding bubble regime and better distribution in the single bubble regime compared to the multiple bubble regime. However, the bottom leakage, i.e., the volatile leakage from the bottom of the VD, should be considered, especially in the single bubble regime.

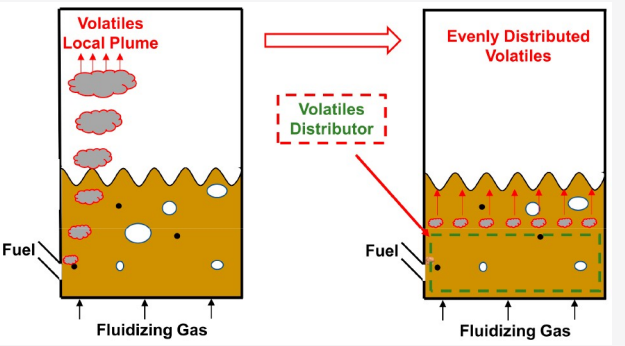

1. INTRODUCTION

In recent years, with the higher frequency and intensity of weather extremes, climate change attracts more and more attention. The CO_2 concentration in the atmosphere increases steadily and reached an annual average of 410 ppm in 2019.[1] In addition, there is still a huge amount of CO_2 emitted every year, which is around 40 Gt of CO_2/year in 2020.[1] As a result of the near-linear relationship between cumulative anthropogenic CO_2 emissions and global warming, the global temperature will continue to increase until the net zero CO_2 emission target is reached. As the Intergovernmental Panel on Climate Change (IPCC) presented in the Sixth Assessment Report, global warming will exceed both 1.5 and 2 °C during the 21st century unless deep reductions in CO_2 and other greenhouse gas emissions occur in the coming decades.[1] Carbon removal technologies are necessary to reach the net zero CO_2 emission to compensate for residual anthropogenic emissions for all scenarios considered by IPCC. Bioenergy carbon capture and storage (BECCS), considered to be the carbon removal technology with the highest potential, will play an important role if climate targets are to be achieved.

Chemical looping combustion of biomass (bio-CLC) is a BECCS technology, which attracts a lot of attention because it has inherent CO_2 capture and avoids costly CO_2 separation processes.[2] There are more than 10 000 h of chemical looping combustion operations with gaseous, liquid, and solid fuels in smaller pilots, which lay a solid foundation for the large-scale application of bio-CLC.[3] Moreover, two conceptual designs of chemical looping combustion of solid fuels with 100 and 1000 MW scale have been published.[4,5] Still, pilot operation results may not be directly applicable to the large-scale units as a result of the different hydrodynamics.[6] Several aspects regarding scaling up based on the successful pilot operations need investigations to facilitate the development and industrialization of bio-CLC.

The inherent CO_2 capture by CLC is achieved by the use of two separated reactors, i.e., the air reactor and the fuel reactor. The oxygen carriers are oxidized by air in the air reactor, and

Special Issue: 2022 Pioneers in Energy Research: Anders Lyngfelt

Received: December 7, 2021
Revised: January 14, 2022
Published: January 28, 2022

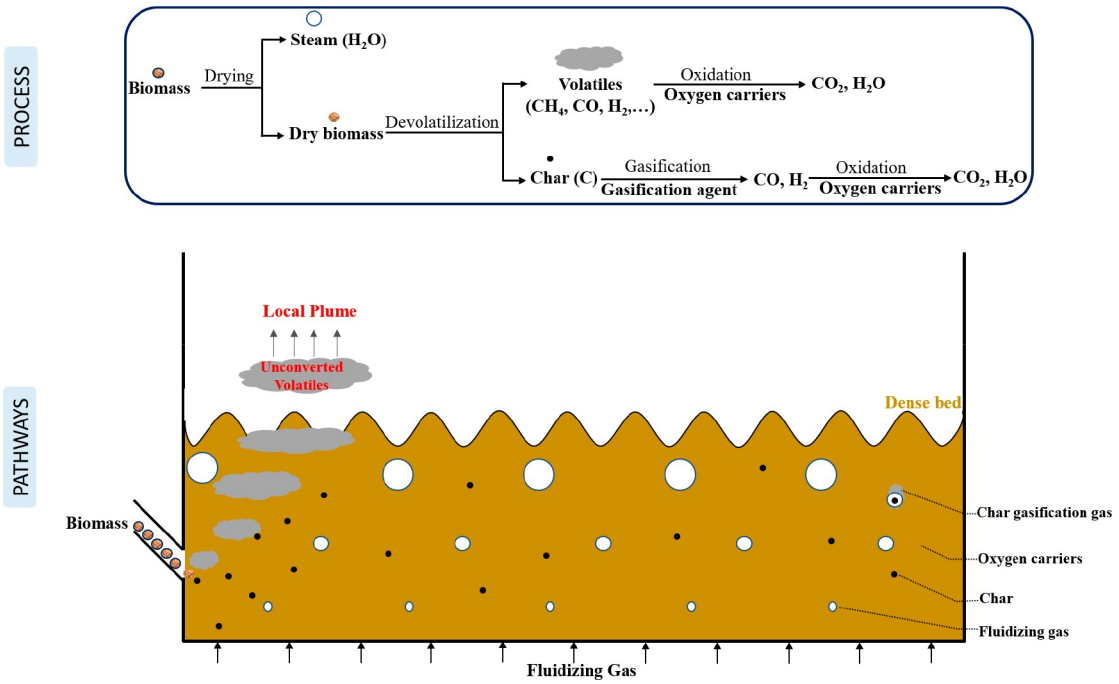

Figure 1. Biomass conversion process and pathways in the fuel reactor.

ideally, there is only the oxygen-depleted air being emitted from the air reactor. The oxidized oxygen carriers are transported to the fuel reactor, where they provide oxygen to convert the fuel. The reduced oxygen carriers are transported back to the air reactor to be regenerated again. Pure CO_2 in flue gas after condensation of the steam can be compressed directly to be transported and then stored underground. Complete combustion of biomass by oxygen carriers can be achieved in the fuel reactor, as indicated by large-scale experiences from chemical looping with oxygen uncoupling (CLOU).[7] However, as a result of the ash contained in solid fuels and the higher volatile content in biomass, commercial operation requires oxygen carriers with lower cost.[2] Another common measure to reach a complete gas conversion is oxygen polishing, which introduces pure oxygen downstream of the fuel reactor and oxidizes the remaining unconverted gases.[8] However, oxygen production is costly and would be a main cost when bio-CLC is applied in industry.[5]

Understanding the biomass conversion process in the fuel reactor and finding out a solution to improve the gas conversion inside would be beneficial to the bio-CLC process. As Figure 1 shows, after the injection of biomass into the hot fuel reactor, the drying and devolatilization happen immediately to generate char and volatiles.[9] Char will go through a slow gasification step, releasing CO and H_2 that will react with oxygen carriers and produce CO_2 and H_2O. Char gasification products could be oxidized more or less completely because of the good contact with the oxygen carriers. A huge amount of volatiles would be formed after devolatilization because biomass has a high content of volatiles. The substantial volatile release in combination with the upward flow direction of the gas may lead to a strong local plume of reducing gas near the biomass injection port. This will yield a limited contact between the volatiles and oxygen carriers in the fuel reactor bed, and thereby, a large amount of volatiles may leave the reactor unconverted. The Damköhler number, which is the ratio of the lateral mixing time of the biomass and the relatively long characteristic time for devolatilization, can also illustrate the fuel mixing behavior.[10] When the Damköhler number is much less than 1, which means sufficient lateral fuel mixing is achieved before the devolatilization is completed, a local volatile plume could be avoided. However, the lateral dispersion coefficient in the order of 10^{-3}–10^{-2} m^2/s[11] on an up-scaled basis and the devolatilization time in the scale of 10^0–10^2 s[12] for larger biomass particles could give the relationship between the Damköhler number (Da) and the characteristic length (L) of the reactor as $Da \sim (5\text{–}500)L^2$. When the characteristic length of the reactor is larger than 0.73 m (averaged from the range of 0.04–1.41 m), Da would be larger than 1. It means that the Damköhler number would be much larger than 1 and the local volatile plume becomes more pronounced with commercial-size reactors with a large cross section. The pilot operations on 1.5, 10, and 100 kW units clearly show that the oxygen demand for the flue gas in the fuel reactor correlates with the volatile content of the solid fuels.[13−15] Ströhle et al.[16] investigated the performance of CLC of Calenturitas coal in a 1 MW_{th} unit and found significant amounts of combustible gases in the fuel reactor exit resulted from the incomplete conversion of devolatilization and gasification products as a result of the limited gas/solid contact in the fluidized bed. Another MW-scale operation on bio-CLC also indicates that the volatile conversion is to a significant extent limited by the mixing.[17] The cross section of the commercial size fuel reactor could have a characteristic length of more than 10 m, which would give a stronger local volatile plume.[5] Hence, a more uniform distribution of volatiles over the cross section of the fuel reactor could help with the gas–solids contact and improve the gas conversion in the fuel reactor.

The concept named "volatile distributor" (VD) was first proposed in a Swedish patent, which could improve the lateral distribution of volatiles in fluidized beds.[18] In principle, the concept includes a downward opened box located in the bottom bed with distribution holes on the sides. The "box"

https://doi.org/10.1021/acs.energyfuels.1c04159
Energy Fuels 2022, 36, 9571−9587

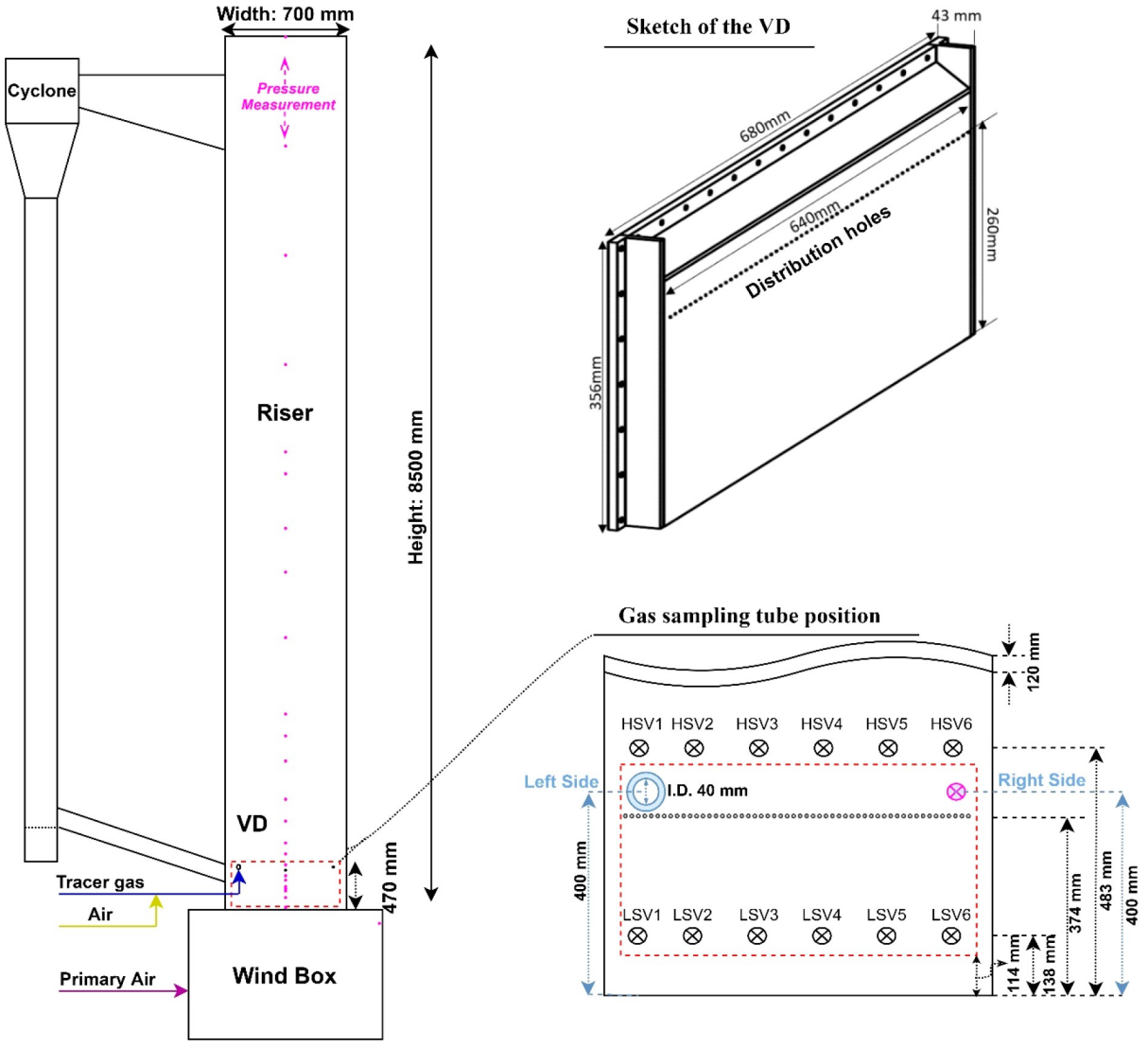

Figure 2. Fluidized bed cold flow model with the VD and the pressure/concentration measurement system (the red dashed-line rectangle shows the position of the VD).

composed of arms allows for a distribution of volatiles over the cross section. The limited open area of the distribution holes on the sides allows for volatiles to spread out across the box and be introduced evenly in the bed, thus avoiding a local plume formation. Lyngfelt and Leckner[5] applied this concept into the conceptual design of a 1000 MW_{th} boiler for CLC of solid fuels. Gogolev et al.[19] implemented a VD in a 10 kW_{th} unit for bio-CLC, which exhibits improved gas conversion efficiency in the fuel reactor. Li et al.[20] introduced the VD concept and evaluated the performance of the VD under different fluidization velocities and flow rates of simulated volatiles in a cold-flow model fluidized bed.

The gas−solids flow is strongly related to the fluidization regime established in the bottom dense bed, where devolatilization, char gasification, and oxidation of the gasification products or volatiles mainly take place. The hydrodynamics of the bottom bed and the performance of different VDs under different fluidization regimes are therefore of great interest. The current pilot operations on CLC of solid fuels are usually conducted with low fluidization velocities, less than 1 m/s.[7,9,16,21−24] However, most publications do not report any information about the pressure drop over the air distributor, which may give different fluidization regimes in the dense bed.[25,26] Furthermore, commercial boilers are normally operated with a relatively smaller pressure drop over the air distributor as a result of economic interests, yielding the single bubble or exploding bubble regime at low and higher fluidization velocities, respectively.[26]

This work aims to investigate the performance of different VD designs under different fluidization regimes and with different air distributors. In this way, the authors want to lay the foundation for future large-scale implementation of the VD concept to improve lateral mixing of the gas and, thereby, gas conversion in fluidized beds, of central importance for technologies like CLC but also applicable for other fluidized bed technologies.

2. MATERIALS AND METHODS

2.1. Experimental System. The fluidized bed unit used, shown in Figure 2, consists of the wind box, the riser, and the cyclone. The length, width, and height of the riser are 700, 120, and 8500 mm, respectively. The front side of the riser is Perspex glass, which allows for visual observation of the inside. There are two different perforated plates used as the air distributor, which have 198 and 1660 holes with

https://doi.org/10.1021/acs.energyfuels.1c04159
Energy Fuels 2022, 36, 9571−9587

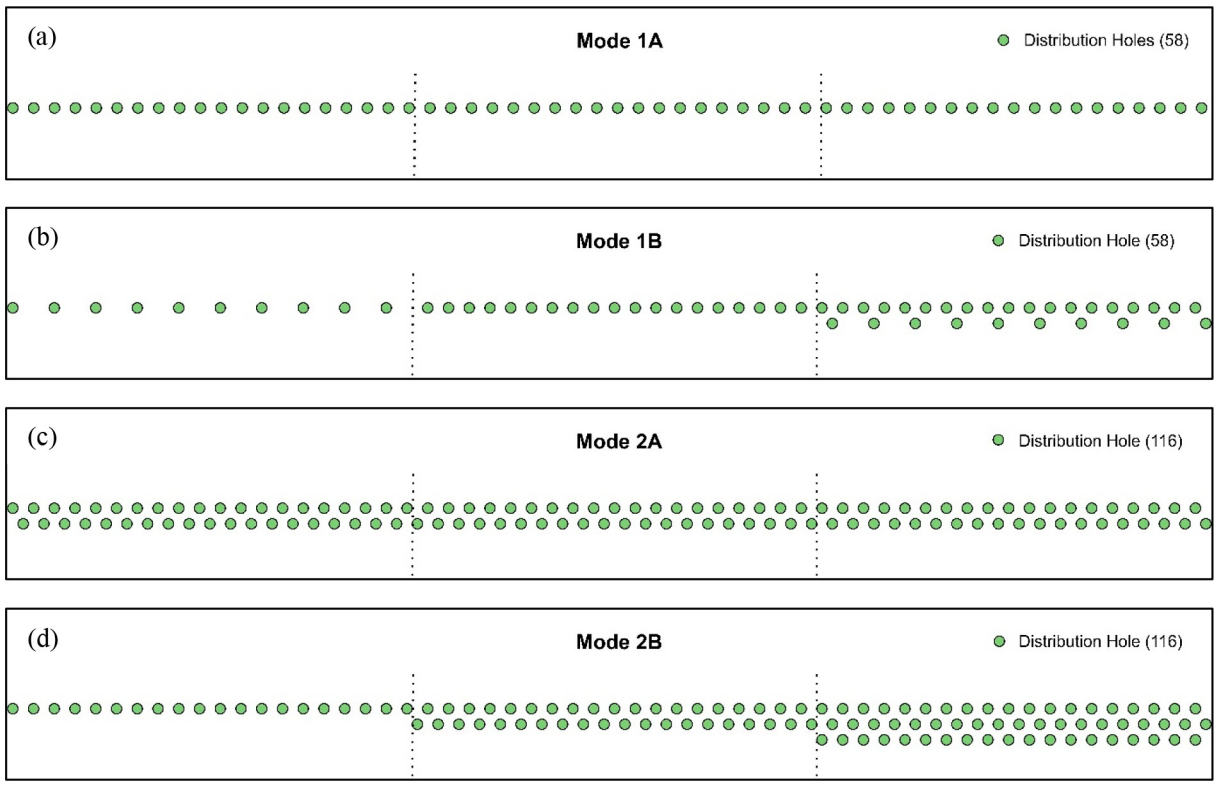

Figure 3. Different designs of VDs with different open areas and hole arrangement modes (modea 1A/1B and 2A/2B have 58 and 116 distribution holes, respectively, with 5 mm diameter).

a diameter of 2 mm, named AD198 and AD1660 in the following, respectively. The open areas of AD198 and AD1660 are 0.7 and 6.2% of the total cross section. The perforated plates are covered by a fine metal mesh to prevent bed materials from dropping into the wind box.

Primary air from two fans was injected into the wind box as the fluidization gas. Another flow of air from the fans together with the tracer gas, which is CO_2, was injected into the riser from the bottom front window to simulate the volatiles.

There are 27 taps in total for pressure measurements, as indicated by the red dots in Figure 2. The one for the wind box was installed at the right side of the wind box. The one for the inside of the VD was installed at the top right corner of the VD, shown as the pink circle with a cross in Figure 2. The remaining ones are distributed along the height of the riser with closer proximity between the ports in the first meter above the air distributor. Huba Control type 663 pressure transmitters are used to measure the differential pressures to obtain the specific pressure at a certain height. All of the pressure measurement data are recorded at a frequency 50 Hz.

Two series of gas sampling tubes are located at the back side of the riser to measure the tracer gas concentration using a gas analyzer, i.e., X-STREAM Enhanced XEGK. The tubes reach 40 mm deep into the bed. The higher series has six ports, i.e., HSV1, HSV2, HSV3, HSV4, HSV5, and HSV6, as shown in Figure 2, which are used to identify the horizontal distribution of the volatiles at a height 109 mm above the distribution hole level of the VD. The lower series consists of six sampling ports, i.e., LSV1, LSV2, LSV3, LSV4, LSV5, and LSV6, which are used to indicate if there is any leakage of volatiles from the bottom of the VD. The lower series is located at a height 24 mm above the lower edge of the VD. The lateral positions of the two series of tubes from the left side are 124, 215, 306, 397, 480, and 579 mm, respectively. The higher and lower level vertical positions are 483 and 138 mm, as shown in Figure 2. One more sampling tube was installed at the top right corner of the VD from the front glass side, which can be used to measure the tracer gas concentration inside the VD. The gas sampled from each tube flows through a filter and enters the gas analyzer for detection at a volume flow of 1 L_n/min. Besides, the gases sampled from the tubes enter the gas analyzer in sequence, i.e., LSV6, LSV5, LSV4, LSV3, LSV2, LSV1, HSV6, HSV5, HSV4, HSV3, HSV2, HSV1, and top right corner of the VD. For each gas sampling tube, the measurement continues 210 s in total with 90 s for stabilization and 120 s for data recording. All of the CO_2 concentrations shown in the following sections are the added tracer gas CO_2 concentrations, i.e., the measured concentration minus the CO_2 concentration in ambient air during that specific experiment.

All control variables and measurement signals were stored by a computer. The software LabVIEW is used to control the flows and record the pressure, concentration, and temperature signals.

2.2. Different Designs of VDs. The concept of VD was introduced in detail in ref 20, where the VD, referred to as mode 1A here, was investigated under different fluidization velocities and volatile flow rates. In this work, different designs of the VD are introduced to achieve a more even volatile distribution along the length of the VD. Different VDs with different open areas and hole arrangements are presented in Figure 3. Modes 1A and 1B have the same open area and number of holes but different hole arrangements. Mode 1A has an evenly distributed open area along the length of the VD. However, mode 1B has a less open area at the left side, i.e., the volatile injection side, but more at the right side, i.e., far away from the volatile injection side. Modes 2A and 2B have similar arrangements as modes 1A and 1B, except that modes 2A and 2B have double the open area as well as double the number of holes.

2.3. Bed Materials. Glass beads are used as bed materials for this study, with a density of 2600 kg/m^3 and a particle size range from 250 to 425 μm, which are similar to the bed materials used in boilers.[27] These solids belong to group B in the Geldart classification. The average particle diameter is 316 μm, corresponding to a single particle terminal velocity of 2.21 m/s. The minimum fluidization velocity is 0.067 m/s.[27] In each experiment, 100 kg of solids was filled into the riser, yielding a fixed bed height of around 0.5 m.

2.4. Experimental Conditions. Li et al.[20] investigated the effectiveness of the VD concept by comparing the performance of the VD to mode 1A and results without VD, giving a basic understanding

https://doi.org/10.1021/acs.energyfuels.1c04159
Energy Fuels 2022, 36, 9571−9587

Table 1. Experimental Conditions with the Air Distributor with 1660 Holes (AD1660)

parameter		without VD		mode 1A			mode 1B			mode 2A			mode 2B		
fluidization velocity	u_0 (m/s)	0.9	3.7	0.9	0.9	3.7	0.9	0.9	3.7	0.9	0.9	3.7	0.9	0.9	3.7
primary air	V_{pa} (m_n^3/h)	235	967	234	235	968	237	237	970	235	236	970	237	237	972
CO_2	V_{CO_2} (L_n/min)	5.6	20.0	5.6	20.0	22.0	5.6	21.6	22.4	5.6	21.6	22.4	5.6	21.6	22.4
simulated volatiles	V_{sv} (m_n^3/h)	20	114	19	102	112	28	111	111	28	112	111	29	111	110
volatile percentage	$V_{sv}/(V_{sv} + V_{pa})$ (%)	8	11	7	30	10	10	32	10	11	32	10	11	32	10

Table 2. Experimental Conditions with the Air Distributor with 198 Holes (AD198)

parameter		without VD			mode 1B			mode 2B		
fluidization velocity	u_0 (m/s)	0.9	0.6	0.6	0.9	0.6	0.6	0.9	0.6	0.6
primary air	V_{pa} (m_n^3/h)	240	166	166	238	166	166	237	166	166
CO_2	V_{CO_2} (L_n/min)	21.6	13.0	30.0	21.6	13.0	30.0	21.6	13.0	30.0
simulated volatiles	V_{sv} (m_n^3/h)	119	77	128	114	70	122	115	72	123
volatile percentage	$V_{sv}/(V_{sv} + V_{pa})$ (%)	33	32	44	32	30	42	33	30	43

of how the VD works under different fluidization velocities. It was found that there is still an uneven lateral distribution of volatiles by the VD with mode 1A, especially for the low fluidization velocity cases. Hence, different designs of VD, i.e., modes 1B, 2A, and 2B, with different open areas and hole arrangements were investigated and compared to the previous results with mode 1A.[20]

The influence of the overall fluidization velocity is investigated using three velocities: 0.6, 0.9, and 3.7 m/s. The concentration of tracer gas, i.e., CO_2, in the simulated volatiles is chosen, first, to ensure that the lowest CO_2 concentration for all of the gas sampling tubes can be distinguished from the CO_2 concentration in air and, second, to ensure that the highest CO_2 concentration is below the maximum detection limit of the gas analyzer. The share of simulated volatiles of the total flow, i.e., the volatile percentage, is also chosen to some certain levels to simulate the different biomass injection rates by controlling the flow rates of primary air and simulated volatiles. The specific experimental conditions with the air distributor equipped with 1660 holes (AD1660) are shown in Table 1.

The pressure drop over the air distributor plays an important role on the fluidization gas distribution above the air distributor and the fluidization regimes in the riser. Therefore, an investigation on the performance of different designs of VD with the air distributor with 198 holes (AD198) was performed to identify how the VD works under different fluidization regimes. The specific operational conditions with AD198 are presented in Table 2.

2.5. Data Analysis. *2.5.1. Solids Concentration.* The solids concentration at a certain height can be estimated by the pressure measurements along the height of the riser. The pressures are the average pressures at different measurement positions during the whole recording period. The average solids concentration, $c_{s,\,h_{1\to 2}}$ (kg/m^3) between two pressure measurement positions h_1 and h_2 can be estimated as follows:[28]

$$c_{s,h_{1\to 2}} = \frac{\frac{|p_{h_1} - p_{h_2}|}{g|h_1 - h_2|} - \rho_{gas}}{1 - \frac{\rho_{gas}}{\rho_s}} \tag{1}$$

2.5.2. Power Spectral Analysis. Power spectral analysis is often used to determine the dominant frequencies and the frequency distributions of pressure fluctuations in the fluidized bed, which can be applied to identify the fluidization regime transitions and validate the hydrodynamic scaling relationships between the pilot- and full-scale units.[29,30] In this work, power spectral analysis of the pressure fluctuation signals by fast Fourier transform (FFT), as a more objective method compared to the time domain analysis, is used to characterize the fluidization regimes.

Assuming that the time series of the variance in the pressure signals is divided into L segments with a length of N_s for each segment. The segments are represented as

$$x_i(n) = x(n + (i-1)N_s), \quad n = 1, 2, ..., N_s, \ i = 1, 2, ..., L \tag{2}$$

The time series signal $x(n)$ estimated as the Fourier transform of the autocorrelation sequence is expressed by

$$F(f) = \sum_{n=1}^{N_s} x(n) e^{-j2\pi nf} \tag{3}$$

The power spectrum density (PSD) can be performed using FFT, which is calculated from

$$P_{xx}^i(f) = \frac{1}{N_s f_s}\left[\sum_{n=1}^{N_s} x(n) e^{-j2\pi nf}\right]^2 \tag{4}$$

Here, the normalization factor $1/(N_s f_s)$ is used. f_s is the sampling frequency.

The average power spectrum is

$$P_{xx}(f) = \frac{1}{L}\sum_{i=1}^{L} P_{xx}^i(f) \tag{5}$$

The number of discrete frequencies tested is proportional to the number of samples in each segment. The frequency resolution or intervals is $\Delta f = f_s/N_s$, i.e., 0.0244 Hz in this work. The highest frequency analyzed (named the Nyquist frequency) is $f_s/2$, i.e., 25 Hz.

The pressure sampling frequency is 50 Hz in this work, which is sufficient to determine the frequency distribution because the major frequency range of pressure fluctuations is normally below 10 Hz.[30] All frequency spectra shown below are based on the average of 32 sub-spectra, of which each has 2048 samples, to ensure sufficient accuracy. The pressure signals are from the measurements at the position 0.03 m above the air distributor and in the wind box.

2.5.3. Standard Deviation of Pressures. The standard deviation of pressures is one method to estimate the fluctuation amplitude, which is calculated as

$$\sigma = \sqrt{\frac{\sum_{n=1}^{N}(x(n) - \overline{P})^2}{N}} \tag{6}$$

where N is the total number of data points, $\overline{P}$ is the average value, and $n = 1, 2, 3, ..., N$.

2.5.4. CO_2 Ratio. In an ideal case, when the injected volatiles are perfectly mixed across the whole cross section, the CO_2 concentration at different positions of the cross section will be the same, which is called the ideal average CO_2 concentration in this work. The ideal average CO_2 concentration is calculated on the basis of the CO_2 flow [MF_{CO_2} (m_n^3/h)], air flow used for simulating volatiles [MF_{SA} (m_n^3/h)], and primary air flow [MF_{PA} (m_n^3/h)] for the main fluidization.

https://doi.org/10.1021/acs.energyfuels.1c04159
Energy Fuels 2022, 36, 9571−9587

$$c_{cal} = \frac{MF_{CO_2}}{MF_{CO_2} + MF_{SA} + MF_{PA}} \quad (7)$$

To compare the horizontal distribution of volatiles in different cases statistically, a parameter named the CO_2 ratio (R) was defined as the ratio between the measured CO_2 concentration [c_m (ppm), with CO_2 in ambient air subtracted] at each measurement position and the ideal average CO_2 concentration in the cross section of the riser [c_{cal} (ppm)].

$$R = \frac{c_m}{c_{cal}} \quad (8)$$

A further analysis based on the CO_2 ratios at different positions of the higher level is conducted to evaluate the overall performance of the different VDs under different operational conditions with different air distributors. Here are the parameters used for the evaluations.

The average CO_2 ratio over the six horizontal measurement positions.

$$\overline{c}(c_1, c_2, ..., c_n) = \frac{\sum_{i=1}^{n} c_i}{n} \quad (9)$$

The standard deviation of the CO_2 ratios.

$$SD = \sqrt{\frac{\sum_{i=1}^{n} (c_i - \overline{c})^2}{n}} \quad (10)$$

The relative standard deviation of the CO_2 ratios.

$$RSD = \frac{SD}{\overline{c}} \times 100\% \quad (11)$$

The ratio between the highest CO_2 ratio (c_H) and the lowest CO_2 ratio (c_L) at the six positions of the higher level is also calculated, which is expressed as c_H/c_L.

2.5.5. Dense Bed Height Estimation Inside the VD. The bed material inside the VD is fluidized by the continuous bottom inflow from the main riser into the VD. The height of the dense bed inside the VD, h_b (see a sketch of the side view in Figure 4), is estimated from pressure measurements. Geometry gives

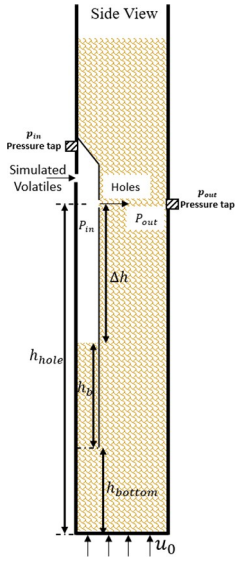

Figure 4. Sketch of the side view of the bottom part of the riser.

$$h_b = h_{hole} - \Delta h - h_{bottom} \quad (12)$$

where h_{bottom} is the distance from the air distributor plate to the lower edge of the VD, h_{hole} is the distance from the distributor plate to the level of distribution holes of the VD, and Δh is the distance between the top of the dense bed surface inside the VD and the level of distribution holes. Δh can be estimated from the pressure difference between the inside VD and the main bed at the hole height, and the measured pressure gradient dp/dh on the outside of the VD is assumed to be similar to that inside the VD.

$$\Delta h = \frac{p_{in} - p_{out}}{|dp/dh|} \quad (13)$$

In this work, the superficial gas velocity inside the VD is also estimated by two methods described in a previous work.[20] The first method is based on an estimation of the gas velocity through the distribution holes.[31] The second method is based on the assumption that the ratio between the average CO_2 concentration inside the VD and the average CO_2 concentration in the riser at the HSV level is corresponding to the ratio between the CO_2 concentration measured at the right top corner of the VD and the CO_2 concentration measured at HSV6.

3. RESULTS AND DISCUSSION

3.1. Solids Concentration Profile. The vertical profile of solids concentration in the riser gives a basic overview of the different fluid dynamic zones established. Figure 5 presents the vertical distributions of the bed materials with different VD configurations, different air distributors, and different flows of fluidization air and simulated volatiles. All cases with fluidization velocities of 0.6 and 0.9 m/s show the existence of the dense bed at the bottom part, because the solids densities measured on the basis of the first two pressure measurements, i.e., at 0.03 and 0.12 m above the air distributor, are above 718 kg/m^3, which means that the bubble volume fraction is lower than 0.5.[27] However, the cases with the fluidization velocity of 3.7 m/s in Figure 5d give lower solids concentrations at the bottom. There is a significant difference in the solids concentration in the bottom region between the case without VD and the cases with different VDs under 3.7 m/s fluidization velocity. With VD, the solids concentration for the cases with 3.7 m/s velocity goes down at first and then goes up until it reaches the main descending trend at 0.47 m, as shown in Figure 5d. Thus, the solids concentration in the bottom region is lower than that in the case without VD. The installation of the VD occupies one-third width of the bottom riser, which results in a higher fluidization velocity and lower solids concentration at the height of VD installation, i.e., 114−470 mm. It is clear that solids are displaced to the region above the VD. The same trend was also found in the previous work.[20] There is no major difference in the solids concentration in the bottom region for the cases with and without the VD when the fluidization velocity is low, i.e., 0.6 or 0.9 m/s. As shown in Figure 5b, there is no big difference in the solids concentration profile at the bottom of the riser when different air distributors (ADs) or different VD configurations are applied. Increase of the volatile flow rate does not give an obvious influence on the solids concentration, as shown in Figure 5c.

3.2. Fluidization Regimes at the Bottom. *3.2.1. Fluidization at the Bottom Riser.* The transparent front plate of the riser provides the opportunity to visualize the fluidization in the riser bottom. Figure 6 illustrates the bubble flow under different operational conditions with different VDs and ADs. It is clear that the bubble size with AD1660 (panels d and e of Figure 6) is much larger than that with AD198 (panels j and k of Figure 6), even though the operational conditions are the same.

https://doi.org/10.1021/acs.energyfuels.1c04159
Energy Fuels 2022, 36, 9571−9587

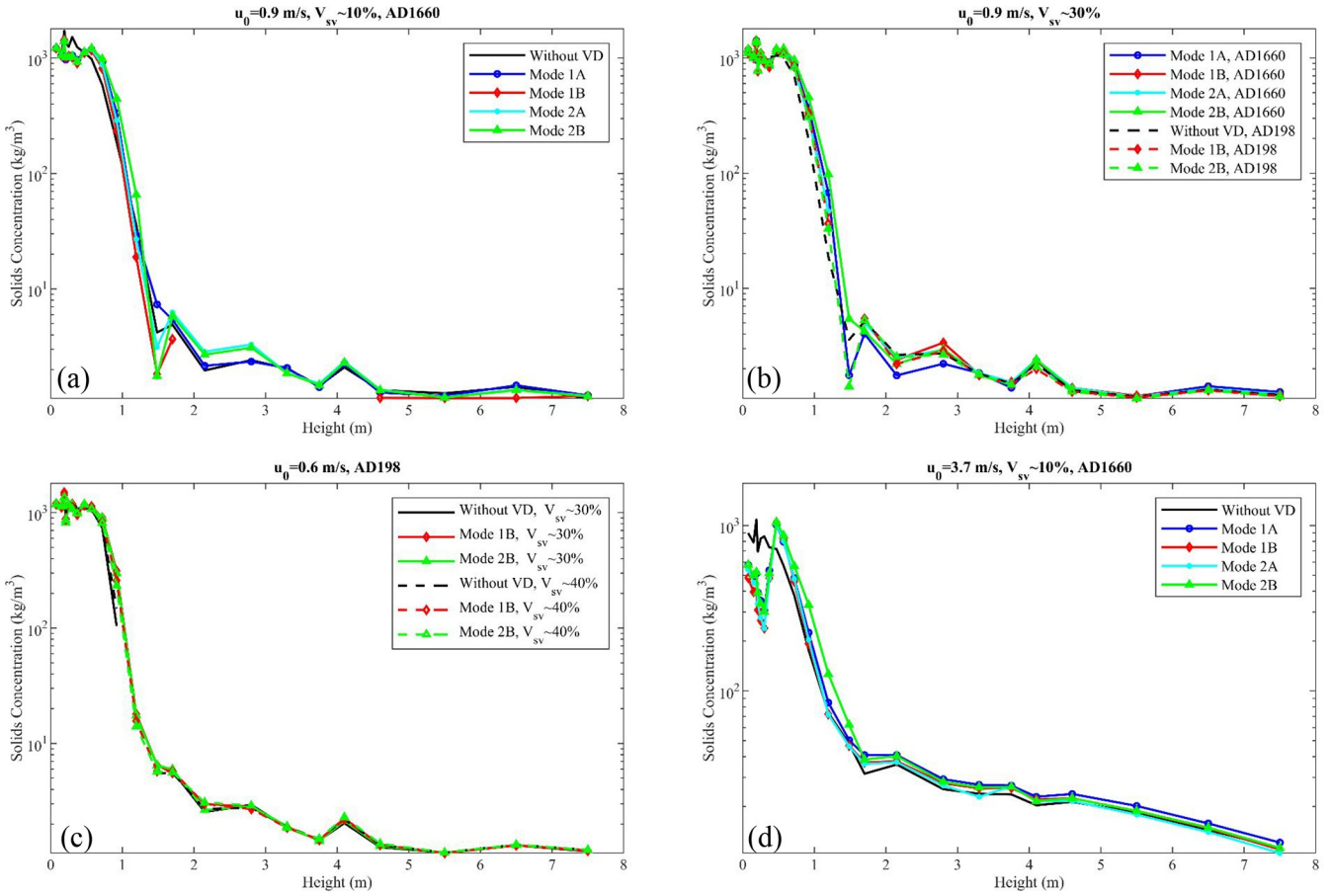

Figure 5. Solids concentration profile along the height of the riser with different AD and VD configurations under different operational conditions.

When the volatile percentage is low, i.e., around 10%, the bubbles with AD1660 form at the riser bottom and grow bigger inside the VD until the particles are carried to the top of the VD (panels a–c of Figure 6). As the volatile flow is increased, i.e., 30% of the total flow (panels d–f of Figure 6), the bubble growth inside the VD is inhibited and the dense bed surface is pushed to a lower height. Thereby, most of the bubbles inside the VD erupt at a middle height of the VD. When the bubbles erupt at the bed surface, the pushed out particles above the bubble are blown to the right side, i.e., the opposing side of volatile inlet, by the injected simulated volatiles. This phenomenon can also be found with smaller bubbles in the cases with AD198 (panels l–o of Figure 6).

According to panels g–i of Figure 6, it is obvious that there is much more diluted solids concentration inside the VD at the bottom when the fluidization velocity is 3.7 m/s compared to other cases. It is consistent with the solids concentration profile results derived from the pressure measurements in the former section. Because a fluidization velocity of 3.7 m/s gives a diluted solids concentration at the bottom and the simulated volatile flow rate is large, a clear left-to-right trend of particles can also be observed under this operational condition.

The videos recorded on the riser bottom under different conditions are available on the internet.[32]

3.2.2. Fluidization Regime Characterization. In this section, the analysis on the pressure fluctuations in the bed and in the wind box is conducted to characterize the fluidization regimes at the bottom riser.

Before the bed is fully fluidized, the pressure fluctuation originates from the blower at a low primary air flow rate. It propagates to the wind box after the attenuation by the gas pipe and valves and then to the bed through the air distributor. However, in the bubbling regime, the pressure in the wind box is mainly influenced by the bubble behavior in the bed.[29]

Examples of the pressure behavior are presented in Figure 7. The pressure variations (panels a and b of Figure 7) show an obvious regularity, which may be caused by large single bubbles (Figure 6d). The frequencies and amplitudes of the pressure variations measured in the wind box and at 0.03 m are similar. This can be illustrated by power spectrum density analysis (panels a and b of Figure 8). Both frequency spectra at the wind box and in the bed show a sharp peak at somewhat below 1 Hz, which are similar to the results from a previous work performed in this experimental system.[26] The sharp peak in the frequency spectrum means a strong periodicity of the formation and eruption of the bubbles, which was characterized as a single bubble regime. In the single bubble regime, most of the bubbles rise up in the center of the bed and the gas flow is discontinuous because of the periodically formed and erupted bubbles. As the fluidization velocity increases from 0.9 to 3.7 m/s, there are more irregular bubbles (panels c and d of Figure 8), which contain more particles than bubbles at lower velocity, i.e., single bubble regime. These irregular bubbles tend to explode at the surface of the bed, which are called exploding bubbles.[26]

When the air distributor is changed to AD198 from AD1660, the pressure variation periodicity is uneven and the

https://doi.org/10.1021/acs.energyfuels.1c04159
Energy Fuels 2022, 36, 9571–9587

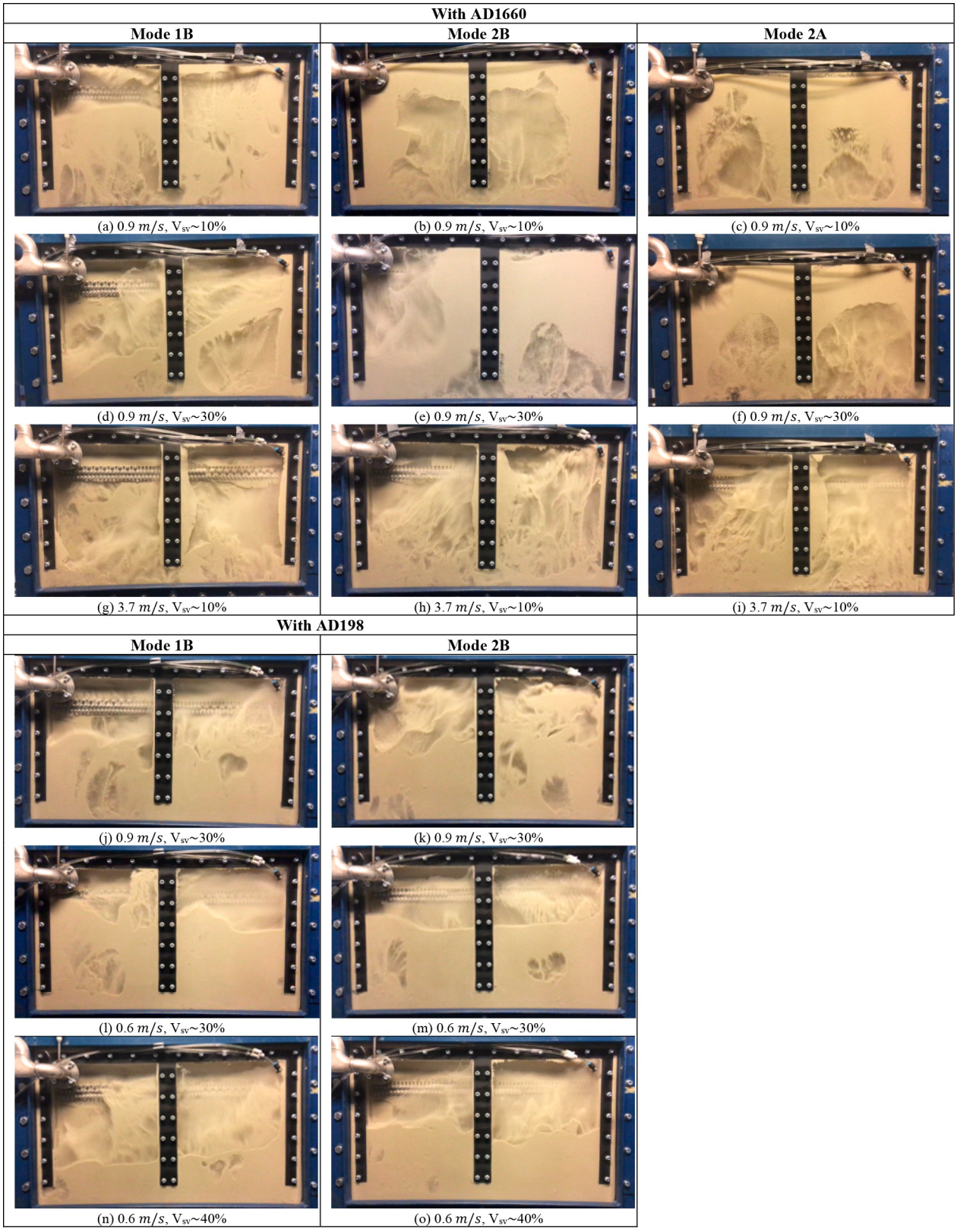

Figure 6. Captured photos of the bottom riser with different VDs and ADs under different experimental conditions.

variation amplitudes differ by a factor of higher than 10 for the pressure in the wind box and at 0.03 m (panels e and f of Figure 7). The pressure vibrates in the ranges of 20.6−21.5 kPa in the wind box and 4−15 kPa at 0.03 m, respectively. The multiple and different sizes of bubbles (Figure 6k) may be the reason for the uneven periodicity. The wide range of frequencies from 1 to 3 Hz in Figure 8f further reflects that there are numerous bubbles with different sizes and formation frequencies in this so-called multiple bubble regime.

https://doi.org/10.1021/acs.energyfuels.1c04159
Energy Fuels 2022, 36, 9571−9587

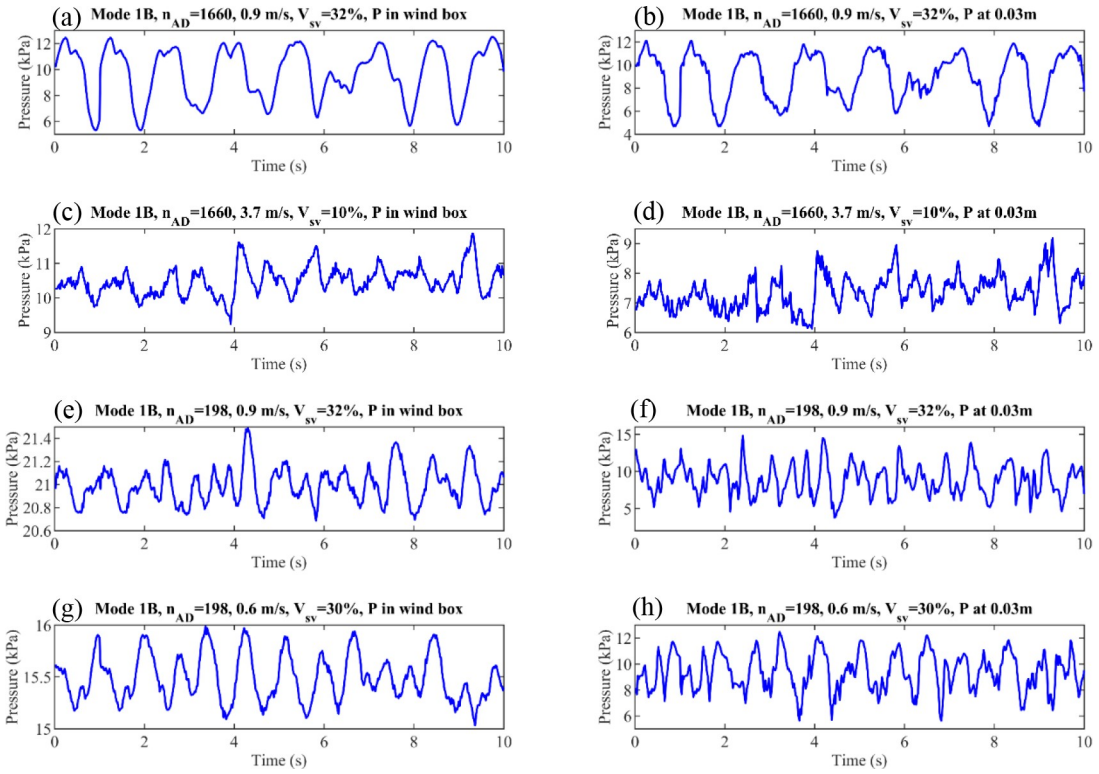

Figure 7. Pressure signal series measured in the wind box and at 0.03 m with VD mode 1B and different ADs under different operational conditions.

The pressure oscillating ranges in the wind box and in the bed are quite similar, i.e., around 7 kPa, under 0.9 m/s fluidization velocity with AD1660. However, they change to around 0.8 and 10 kPa, respectively, under 0.9 m/s fluidization velocity with AD198. This is caused by the different pressure drops over the air distributor, as presented in Table 3, which increases from 0.58 to 11.74 kPa. When the resistance of the air distributor is low, the local fluidization air flow rate is higher where the pressure right above the distributor is low. For the AD1660 case, the air distributor pressure drop is less than 10% of that of the entire bed. The fluidization air tends to flow continuously into the bubble formed above the air distributor and make the large single bubble formed in the AD1660 case.

The correlation between the pressures in the wind box and at 0.03 m in the bed was analyzed on the basis of the CORREL function in Excel. The correlation coefficient is used to determine how well the pressures between in the wind box and in the bed are correlated. As a result of the lower pressure drop across the AD1660 compared to AD198, the interaction between the bed and the air supply system is stronger, which can be indicated by the correlation coefficients in Table 3. The correlation coefficients in the AD1660 case are close to 1, and those in the AD198 case are close to 0, which means that the pressures in panels a and b or panels c and d of Figure 7 are much more correlated than those in panels e and f or panels g and h of Figure 7. The stronger interaction would be another way to distinguish the exploding bubble regime from the multiple bubble regime, because the multiple bubble regime has less correlated pressures in the wind box and in the bed and larger difference in the frequency spectrum between in bed and in the wind box, as shown in Figure 8.

When the fluidization velocity is lowered from 0.9 to 0.6 m/s with AD198, the pressure fluctuates with lower frequency and the amplitude is lower (panels g and h of Figure 7). The pressure oscillating range at 0.03 m is 6−12 kPa in the 0.6 m/s case compared to 5−15 kPa in the 0.9 m/s case. Similarly, the PSD at 0.9 m/s is almost twice than that at 0.6 m/s (panels f−h of Figure 8). These changes are caused by different bubble sizes and displacement velocities as a result of higher fluidization velocity in the bubbling regime with the same air distributor. The frequency spectra of pressure fluctuations in these two cases show a similar fluidization regime, except for the slight difference in the fluctuation frequency. The frequency distribution under 0.6 m/s is narrower than that under 0.9 m/s, because Δp_{AD} changes from 11.74 to 5.55 kPa and the pressure ratio decreases from 134 to 61%, as shown in Table 3.

It is clear that the increased pressure drop over the air distributor by either high fluidization velocity or less open area of the air distributor ensures more uniform distribution of fluidization gas, i.e., wider frequency distribution range.

3.2.3. Pressure Difference between Inside and Outside the VD. Table 4 shows the pressures inside and outside the VD with different VD configurations and air distributors under different fluidization velocities and simulated volatile flow rates. In general, the average pressure outside the VD is always lower than that inside the VD, which means that the dense bed surface inside the VD is always below the level of the distribution holes.

As a consequence of doubling the open area of the VD, i.e., from mode 1B to mode 2B, the pressure difference between inside and outside of the VD, i.e., $P_{in} - P_{out}$, becomes smaller for both air distributors as Table 4 shows. However, this is not observed at high fluidization velocity because the solids concentration at the bottom is low and there is no obvious dense bed inside the VD. In addition, the average pressure

https://doi.org/10.1021/acs.energyfuels.1c04159
Energy Fuels 2022, 36, 9571−9587

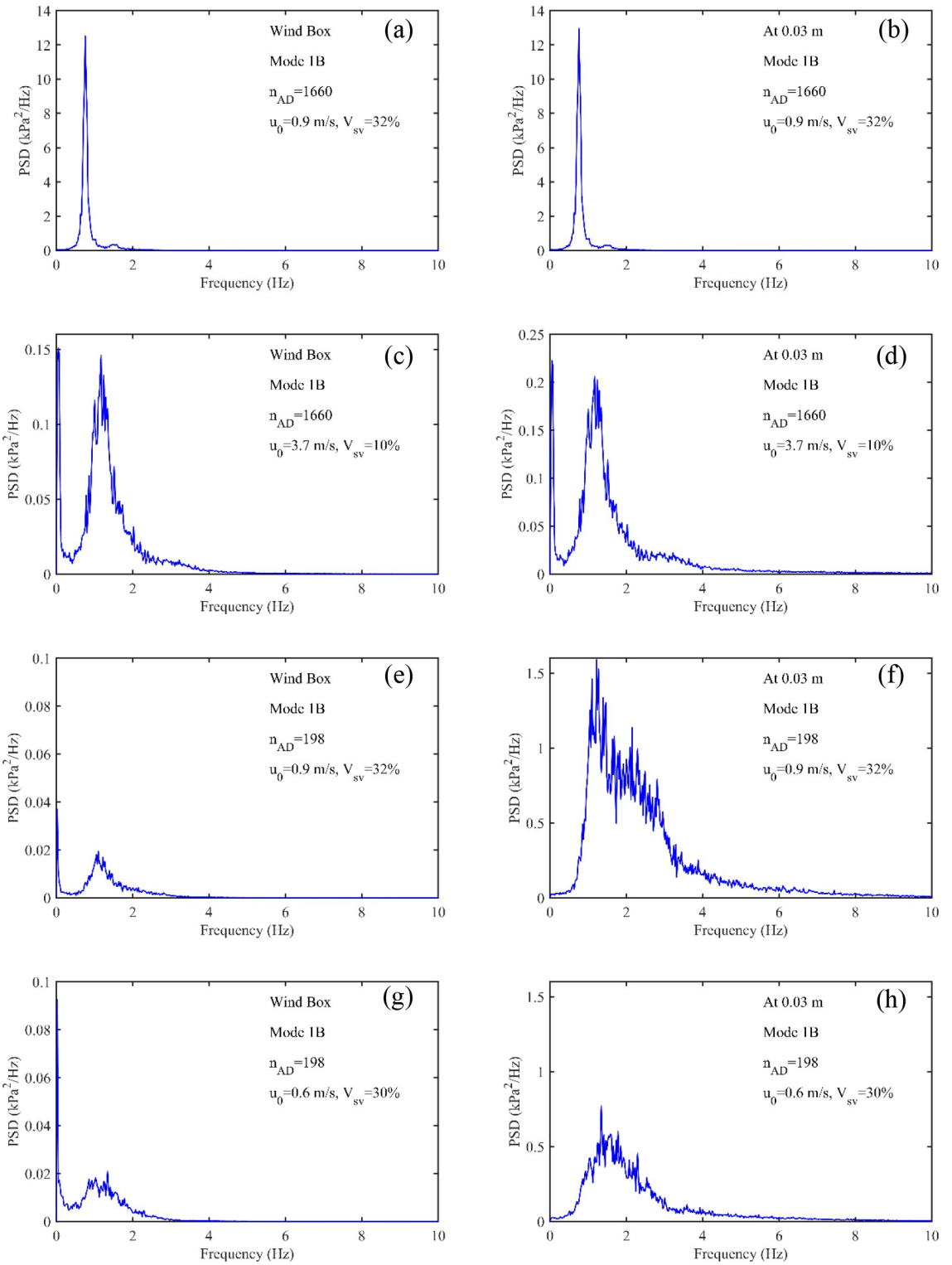

Figure 8. Power spectrum density of the pressure signal in the wind box and in the bed at 0.3 m with different ADs.

drop under similar operational conditions with AD1660 does not change very much when the VD is changed from mode 2B to mode 2A.

Table 4 also shows that a higher flow rate of simulated volatiles generally gives a higher standard deviation of the pressure inside the VD, i.e., P_{in}, which indicates more vigorous oscillations of the bed inside the VD.

The standard deviation of the pressure outside the VD, with the sampling location as indicated in Figure 4, decreases significantly when the AD is changed from a low to high pressure drop, i.e., as the fluidization regime goes from the single bubble to multiple bubble regime. However, the standard deviation of the pressure difference, i.e., $P_{in} - P_{out}$, in the single bubble regime is lower than that in the multiple bubble regime, which is caused by the higher correlation of

https://doi.org/10.1021/acs.energyfuels.1c04159
Energy Fuels 2022, 36, 9571−9587

Table 3. Analysis of Pressures over the Air Distributor and the Whole Riser

parameter		AD1660		AD198	
fluidization velocity	u_0 (m/s)	0.9	3.7	0.9	0.6
gauge pressure in the wind box	$p_{windbox}$ (kPa)	9.50	10.43	20.77	14.89
gauge pressure at the bottom of the riser	p_0 (kPa)	8.92	7.45	9.04	9.34
gauge pressure at the top of the riser	p_8 (kPa)	0.27	0.89	0.29	0.17
pressure drop over the air distributor	Δp_{AD} (kPa)	0.58	2.98	11.74	5.55
pressure drop along the riser	Δp_{riser} (kPa)	8.65	6.56	8.75	9.16
pressure ratio	$\Delta p_{AD}/\Delta p_{riser}$ (%)	7	45	134	61
correlation coefficient		0.98	0.85	0.21	0.26

pressure fluctuations between inside and outside the VD in the single bubble regime compared to the multiple bubble regime.

3.3. Horizontal Distribution of Volatiles. *3.3.1. Tracer Gas Concentration Signals.* Figure 9 presents three examples of the CO_2 concentration signals recorded at different measurement positions under similar operational conditions with different VD configurations, cf. Figure 3, and without VD. A higher CO_2 concentration was detected at positions that are close to the simulated volatile injection port, i.e., HSV1 and HSV2, in the case without VD, i.e., Figure 9a. The impact of inserting a VD (mode 1A in this case) is shown in Figure 9b, yielding a more even CO_2 distribution at the higher level of measurement positions. As for the different arrangement of the holes, mode 1B in Figure 9c yields a higher CO_2 concentration in locations further away from the simulated volatile injection port, as compared to mode 1A.

3.3.2. Performance of VDs with Different Configurations in the Single Bubble Regime. According to the definition of the CO_2 ratio, it would be 1 under ideal conditions of mixing. However, as a result of the imperfect lateral dispersion and mixing, the CO_2 ratio is larger than 1 at the simulated volatile injection side and lower than 1 at the opposing side. The average CO_2 ratio over the six horizontal measurement positions is generally close to 1, as shown in Table 6, which means that the CO_2 concentrations measured at the six positions are representative of the real CO_2 distribution at this level. However, the average CO_2 ratio deviates from 1 under some operating conditions, in particular in single and exploding bubble regimes. There is a reason to expect a deviation between measured and actual average CO_2 concentrations. According to the two-phase theory of fluidization, there is a small flow of gas moving upward in the dense phase and a larger flow moving upward at a much higher velocity through bubbles[33] and bypass flow.[34] For the gas extracted by the suction probes, the rapidly moving gas will not be represented in proportion to its flow and, thus, underrated. This rapidly moving gas flow originates from the bottom air and would therefore start with a low CO_2 concentration. The ratio measured will then be dependent upon the extent to which the gas added to the VD is sucked into this rapid gas flow. Generally, it would be expected that more of the gas from the VD goes into the dense phase when the pressure drop over the distribution holes is high, i.e., modes 1A and 1B, and that more of the VD gas goes into the rapid gas flow when there is no VD, which also agrees with observations. Furthermore, the rapid bypass flow would be greater in the single bubble and

Table 4. Average and Standard Deviation Values of Pressures Inside and Outside the VD with Different VD Configurations and ADs

AD	Distribution Hole Arrangement	Fluidization velocity, m/s	Volatiles percentage	p_{in}, kPa		p_{out}, kPa		p_{in}-p_{out}, kPa	
		u_0	$V_{sv}/(V_{pa}+V_{sv})$	Average	StD	Average	StD	Average	StD
1660	Mode 1B	0.9	10%	6.23	1.10	4.90	1.54	1.33	1.10
			32%	7.16	1.79	5.27	1.50	1.89	1.20
		3.7	10%	7.06	0.62	6.07	0.69	0.99	0.36
	Mode 2B	0.9	11%	6.74	1.73	5.87	1.37	0.87	1.17
			32%	7.15	2.03	6.02	1.59	1.13	1.35
		3.7	10%	7.88	0.89	6.87	0.96	1.00	0.38
	Mode 2A	0.9	11%	6.03	1.63	5.19	1.35	0.84	1.05
			32%	6.29	2.00	5.24	1.65	1.05	1.20
		3.7	10%	6.89	0.63	6.00	0.70	0.89	0.32
198	Mode 1B	0.9	32%	7.12	2.16	5.30	0.36	1.82	2.08
		0.6	30%	6.47	1.50	5.25	0.49	1.21	1.38
			42%	6.74	1.63	5.01	0.42	1.73	1.53
	Mode 2B	0.9	33%	6.24	2.29	5.20	0.54	1.04	2.16
		0.6	30%	6.02	1.60	5.21	0.64	0.81	1.43
			43%	5.94	1.83	4.92	0.54	1.02	1.69

https://doi.org/10.1021/acs.energyfuels.1c04159
Energy Fuels 2022, 36, 9571−9587

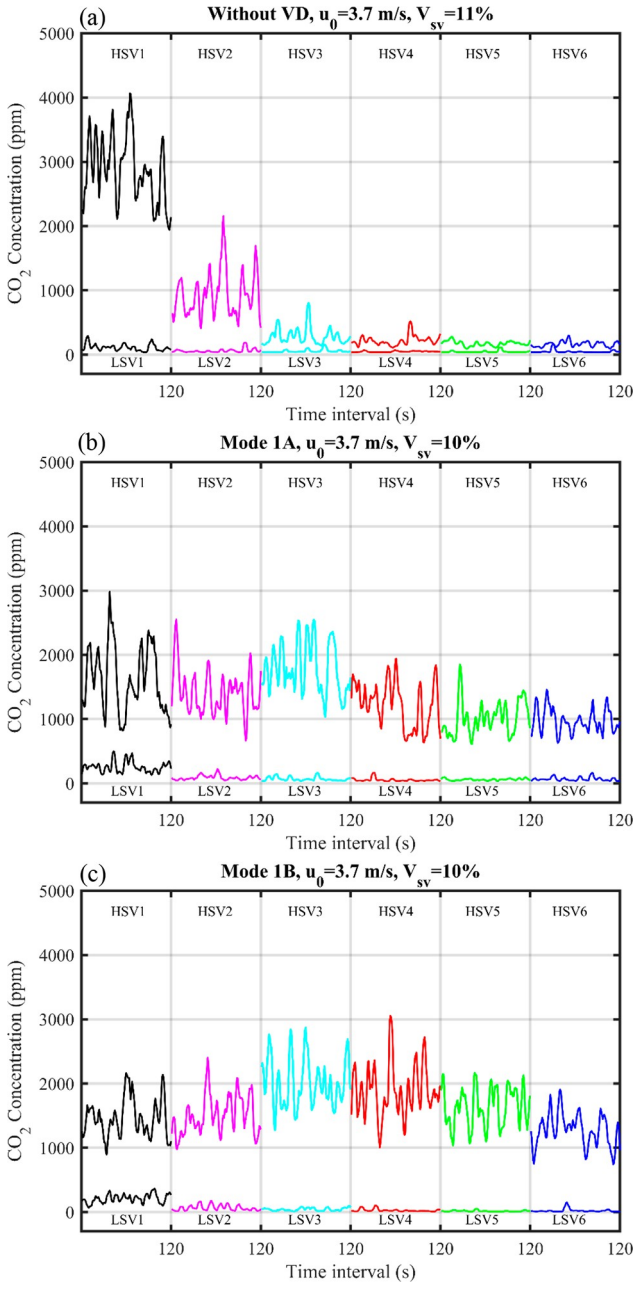

Figure 9. CO_2 concentration signals at different measurement positions with or without the VD.

exploding bubble regimes than in the multiple bubble regime. This agrees with Figure 12, where the multiple bubble regime has a somewhat lower average CO_2 ratio.

Figure 10 presents the CO_2 ratios at different positions with VDs of different configurations in the single bubble regime. Modes 1B and 2B give a more uniform horizontal distribution at the higher level compared to modes 1A and 2A. Because the simulated volatiles are injected from the left side, more simulated volatiles would be distributed through the holes near the injection port as a result of the imperfect mixing inside the VD when the distribution holes are evenly distributed, i.e., modes 1A and 2A. When the configuration of the distribution holes is uneven, i.e., modes 1B and 2B, more of the injected simulated volatiles are forced to flow to the right side, thus providing a more even distribution along the length of the distributor.

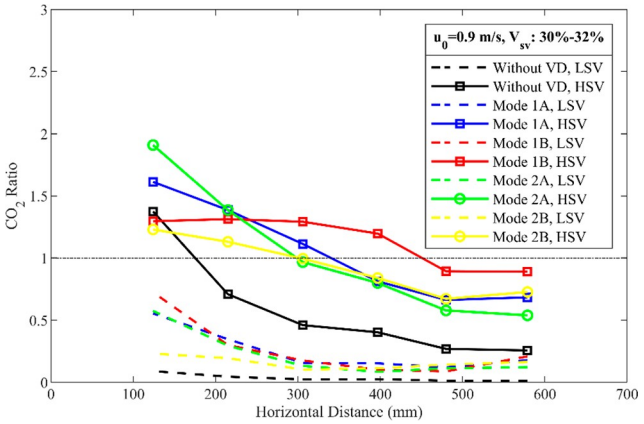

Figure 10. Performance of VDs with different configurations with AD1660.

Modes 1A and 1B give a more even horizontal distribution at the higher level compared to modes 2A and 2B, respectively. Less open area gives a higher pressure drop over the distribution holes and, thus, lower flow. This means that the dilution of the gas in the VD with gas coming from below is reduced. Assuming that the gas added from below is equal along the length of the VD, it is obvious that the dilution will reduce the CO_2 concentration along the length of the VD. Thus, the concentration of CO_2 in the gas going through the holes will fall more along the length of the VD when dilution is increased. This fall will give a less even distribution.

There are mainly two sources of the simulated volatiles at the lower level, i.e., leakage from the bottom of the VD and back mixing near the walls.[20] As Figure 10 shows, the horizontal distributions at the lower level are similar for modes 1A and 2A. However, there is a large decrease in the CO_2 ratio at LSV1 from mode 1B to mode 2B, even though the CO_2 ratio at HSV1 is similar, which indicates that a larger open area of the distribution holes of mode 2B reduces the bottom leakage of the VD dramatically.

In general, uneven hole distribution and smaller hole area provide a more even horizontal profile of the simulated volatiles. However, the bottom leakage should be considered, because less open area on VD gives a greater risk of bottom leakage.

3.3.3. Influence of Simulated Volatile Flow Rates on the VD Performance. Figure 11 shows the horizontal distribution of the simulated volatiles by modes 1B and 2B at a fluidization velocity of 0.9 m/s with different simulated volatile flow rates. Increased simulated volatile flows result in significant improvement of the horizontal distribution at the higher level, especially for mode 1B, which has less open area than mode 2B. The CO_2 ratio at LSV1 is high when the simulated volatile flow is high for mode 1B, even though the corresponding CO_2 ratio at HSV1 is much lower than with low volatile flow. This indicates increased leakage when the simulated volatile flow is increased.

Hence, more volatiles would improve the uniformity of the horizontal distribution and also increase the bottom leakage.

3.3.4. Influence of Fluidization Regimes on the VD Performance. In this work, the exploding bubble regime was achieved by increasing the fluidization velocity to 3.7 m/s from 0.9 m/s with AD1660. Moreover, the multiple bubble regime was achieved by changing the air distributor to AD198 from AD1660. Figure 12 shows that the VD provides a better

https://doi.org/10.1021/acs.energyfuels.1c04159
Energy Fuels 2022, 36, 9571−9587

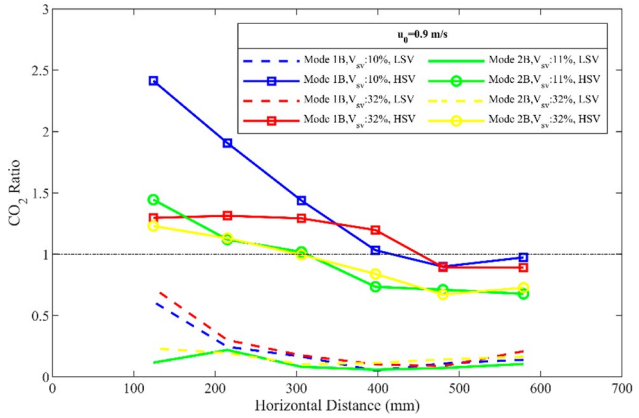

Figure 11. Performance of VDs under different simulated volatile flow rates.

horizontal distribution in the single bubble regime and exploding bubble regime than in the multiple bubble regime.

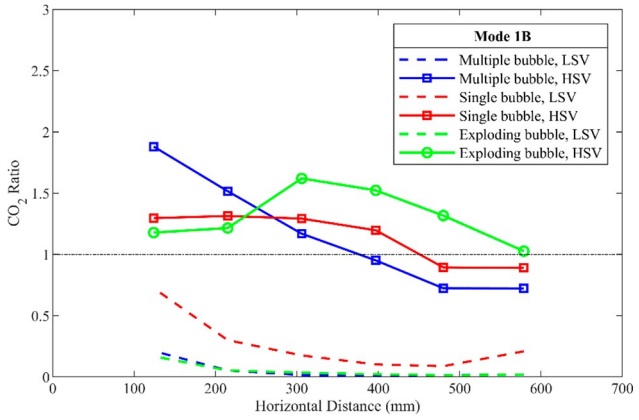

Figure 12. Performance of VD mode 1B under different fluidization regimes (single bubble regime, u_0 = 0.9 m/s and V_{sv} = 32% with AD1660; multiple bubble regime, u_0 = 0.9 m/s and V_{sv} = 32% with AD198; and exploding bubble regime, u_0 = 3.7 m/s and V_{sv} = 10% with AD1660).

Furthermore, the bottom leakage from the VD in the single bubble regime is larger, especially at LSV1, which is near the simulated volatile injection side, compared to the multiple bubble regime and exploding bubble regime. This is because of the larger single bubbles formed at the riser bottom and the more violent bed fluctuations inside the VD.

3.3.5. Influence of Fluidization Velocities in the Multiple Bubble Regime. There is no significant influence on the horizontal distribution of volatiles from the fluidization velocity decreasing from 0.9 to 0.6 m/s in the multiple bubble regime as Figure 13 shows. However, the CO_2 ratio at LSV1 is reduced to 0 by decreasing the fluidization velocity. It is because a lower fluidization velocity decreases the back mixing of gases.[35]

3.4. Fluidization Inside the VD. Table 5 shows the estimated dense bed height and fluidization velocity inside the VD. As seen, the height of the dense bed inside the VD decreases with the increase of the simulated volatile percentage. The correlation is weaker for VDs with a larger open area.

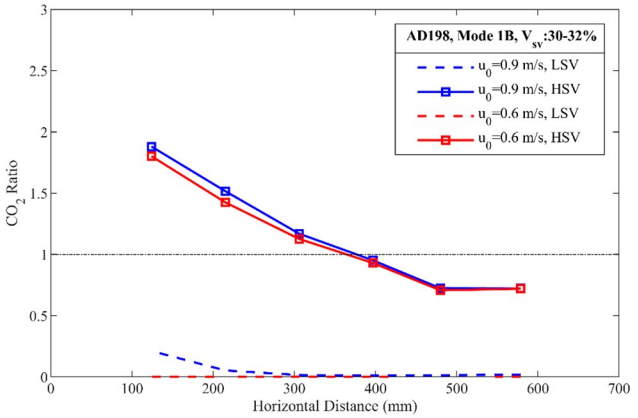

Figure 13. Performance of VD mode 1B under different fluidization velocities in the multiple bubble regime.

Furthermore, when the fluidization velocity is increased from 0.6 to 0.9 m/s in the multiple bubble regime and the simulated volatile percentage in the riser is kept similar, the dense bed height inside the VD decreases. However, it decreases less when the open area of the distribution holes of the VD is larger. This finding is similar to previous work when the fluidization velocity is increased from 1 to 3 m/s with AD1660. The same percentage of simulated volatiles but with increased flow rates of fluidization air and simulated volatiles gives a higher pressure drop over the distribution holes. At the same time, the increased fluidization velocity gives less pressure gradient outside the VD at the bottom, which would make the dense bed height lower.

Moreover, given a number of holes in the VD, their distribution and fluidization regimes (single or multiple bubbles) do not give a big difference in the pressure drop over the holes and the estimated bed height inside the VD under similar conditions.

Table 5 presents the results calculated on the basis of the two methods described in section 2.5. There are negative values for the bottom air flow rates and the fluidization velocity inside the VD for the fluidization velocity of 3.7 m/s, which could be explained by inaccuracy of the pressure measurements or the parameters chosen for the calculation, i.e., the orifice discharge coefficient. However, the trends observed from the values of the fluidization velocity inside the VD and the bottom air flow through the distribution holes of the VD make sense.

The fluidization velocity inside the VD decreases with a raised simulated volatile fraction under otherwise similar conditions. When both the overall fluidization velocity and the simulated volatile flow are raised proportionally using AD198, i.e., the 30% case, the fluidization velocity inside the VD decreases as well. This trend is the same as in the previous work.[20]

Further, the different VD configurations do not affect the fluidization velocity inside the VD that much when the operational conditions are similar. However, the fluidization velocity inside the VD decreases when the air distributor is changed from AD1660 to AD198 under the same operational conditions and with the same VD according to the first calculation method. For the second calculation method, the fluidization velocity inside the VD decreases for the mode 1B case but increases slightly for the mode 2B case. Because the hole arrangements of the VD modes 1B and 2B have less open

https://doi.org/10.1021/acs.energyfuels.1c04159
Energy Fuels 2022, 36, 9571−9587

Table 5. Fluidization Parameters Inside the VD

Air distributor		AD1660												AD198					
VD holes arrangement		Mode 1A			Mode 1B			Mode 2A			Mode 2B			Mode 1B			Mode 2B		
Fluidization velocity	u_0 [m/s]	0.9		3.7	0.9		3.7	0.9		3.7	0.9		3.7	0.9	0.6		0.9	0.6	
Volatiles fraction	$\frac{V_{sv}}{V_{sv}+V_{pa}}$	7%	30%	10%	10%	32%	10%	11%	32%	10%	11%	32%	10%	32%	30%	42%	33%	30%	43%
Simulated volatiles flow	V_{sv} [m_n^3/h]	18.71	101.79	112.02	27.70	111.03	110.93	28.48	111.98	110.78	29.03	110.93	109.78	114.04	70.00	122.14	114.99	71.95	123.05
Pressure drop over distribution holes	$P_{in}-P_{out}$, [kPa]	1.12	1.87	1.17	1.33	1.89	0.99	0.84	1.05	0.89	0.87	1.13	1.00	1.82	1.21	1.73	1.04	0.81	1.02
Pressure gradient	dp/dh, [kPa/m]	10.38	9.81	-	10.44	9.80	-	10.50	10.24	-	10.43	10.14	-	9.94	10.66	10.39	9.91	10.59	10.31
Dense bed height inside VD	h_b, [m]	0.15	0.07	-	0.13	0.07	-	0.16	0.17	-	0.18	0.15	-	0.08	0.15	0.09	0.15	0.18	0.16
Orifice discharge coefficient	C_d	0.6																	
Density of gases through orifices	ρ_{gas} [kg/m^3]	1.19																	
Orifice velocity	v_i [m/s]	26.03	33.63	26.62	28.33	33.85	24.45	22.52	25.27	23.19	22.89	26.17	24.65	33.24	27.08	32.36	25.11	22.16	24.84
Open area of the orifices	A [m^2]	1.138×10^{-3}						2.276×10^{-3}						1.138×10^{-3}			2.276×10^{-3}		
Orifice gas flow	$V_{orifice}$ [m_n^3/	106.62	137.79	109.04	116.08	138.67	100.17	184.53	207.03	190.02	187.57	214.41	201.98	136.16	110.94	132.56	205.73	181.54	203.54
Bottom air flow	V_{ba} [m_n^3/h]	87.91	35.99	-	88.38	27.63	-	156.05	95.05	79.25	158.54	103.48	92.20	22.13	40.94	10.41	90.74	109.59	80.50
Fluidization inside the VD	u_{VD} [m/s]	1.03	0.42	-	1.04	0.32	-	1.83	1.11	0.93	1.86	1.21	1.08	0.26	0.48	0.12	1.06	1.28	0.94
CO_2 concentration measured inside VD	$c_{VD,mea}$ [ppm]	2302	5763	7270	2690	7552	8763	1705	4283	3600	2560	7231	7162	6853	4512	9871	5000	3525	7702
Average CO_2 concentration inside VD	$c_{VD,avg}$ [ppm]	4323	8980	10099	3992	9770	11220	3861	8329	11036	3603	9308	10631	11026	6937	14144	8368	7525	12386
Bottom air flow	V'_{ba} [m_n^3/h]	58.88	31.81	18.67	56.32	21.62	9.27	58.39	43.63	10.99	64.07	28.30	16.64	3.50	42.05	5.13	39.88	31.66	22.30
Fluidization inside the VD	u'_{VD} [m/s]	0.69	0.37	0.22	0.66	0.25	0.11	0.68	0.51	0.13	0.75	0.33	0.19	0.04	0.49	0.06	0.47	0.37	0.26

Table 6. Statistical Evaluation on the Performance of Different VDs under Different Experimental Conditions

Air distributor	VD holes arrangement	Fluidization velocity u_0 [m/s]	Simulated volatiles percentage V_{sv}	Open area of the VD A [m^2]	Average CO_2 ratio	Standard deviation	Relative standard deviation	Highest/Lowest Concentration
AD1660	Mode 1A	0.9	7%	1.138×10^{-3}	1.21	0.57	47%	3.5
			30%		1.01	0.36	36%	2.51
		3.7	10%		1.07	0.25	23%	1.86
	Mode 1B	0.9	10%		1.44	0.55	38%	2.69
			32%		1.14	0.18	16%	1.48
		3.7	10%		1.31	0.2	16%	1.58
	Mode 2A	0.9	11%	2.276×10^{-3}	1.25	0.73	59%	4.86
			32%		1.01	0.48	48%	3.64
		3.7	10%		1.3	0.59	45%	4.81
	Mode 2B	0.9	11%		0.95	0.28	29%	2.14
			32%		0.92	0.21	22%	1.85
		3.7	10%		1.14	0.31	28%	2.13
AD198	Mode 1B	0.9	32%	1.138×10^{-3}	1.16	0.42	36%	2.56
		0.6	30%		1.12	0.39	35%	2.52
			42%		1.02	0.29	28%	2.2
	Mode 2B	0.9	33%	2.276×10^{-3}	0.95	0.39	42%	2.95
		0.6	30%		0.97	0.53	55%	4.38
			43%		0.94	0.36	38%	2.72

area at the left side and more open area at the right side, the second calculation method for the fluidization velocity inside the VD is considered less appropriate. Hence, the first method is considered more relevant. There is less bottom air flow through the VD in the multiple bubble regime than in the single bubble regime when the operational conditions and the VD are the same.

3.5. Overall Influences of Different ADs and VDs. Table 6 summarizes the results of the experiments with different VD configurations. The standard deviation of the CO_2 ratios at different horizontal positions, together with the relative standard deviation and the ratio between the highest and lowest concentration, gives an overall evaluation on the uniformity of the horizontal distribution of the simulated volatiles by different VDs.

It shows that the VD in modes 1B and 2B has better overall performance for the horizontal distribution. Furthermore, the SD, RSD and c_H/c_L are smallest for the exploding bubble

https://doi.org/10.1021/acs.energyfuels.1c04159
Energy Fuels 2022, 36, 9571−9587

regime, middle for the single bubble regime, and largest for the multiple bubble regime.

Because the pressure drop over the VD distribution holes are similar between the single bubble regime and multiple bubble regime, the gas mixing inside the VD is mainly affected by the bubble regime and larger single bubbles in the main riser give better gas mixing with simulated volatiles compared to the smaller multiple bubbles. Another potential reason is that the turbulent horizontal volatile dispersion is improved by the more pronounced coalescence of larger bubbles in the single bubble regime compared to that in the multiple bubble regime.

Generally, the VDs with less open area or larger simulated volatile flow give a better horizontal tracer distribution across the cross section by comparing the values of SD, RSD, and c_H/c_L in Table 6.

4. CONCLUSION

The fluidization regime (single, multiple, or exploding bubble regime) established at the dense bottom region has a strong impact on the performance of the VD and, thus, has implications on the design and practical application of the VD. Generally, the VD works best in the exploding bubble regime.

Under both single and multiple bubble regimes, larger release of volatiles will cause more pronounced bed oscillations inside the VD and decrease the bed level inside the VD as a result of the higher pressure drop over the distribution holes of the VD. A doubling of the open area of the VD would lower the pressure drop over the inside and outside of the VD, which moderates the decrease in bed level inside the VD. However, different VD hole arrangements, i.e., even or uneven hole distribution, do not affect the VD bed pressure difference, the gas velocity, or dense bed height inside the VD significantly.

The multiple bubble regime gives lower pressure fluctuation amplitude outside the VD compared to the single bubble regime because of the smaller bubbles formed. However, the standard deviation of $P_{in} - P_{out}$ increases because the pressure fluctuations inside and outside the VD are less correlated in comparison to the single bubble regime. Less bottom air and lower fluidization velocity inside the VD are achieved when the single bubble regime is changed to the multiple bubble regime under the similar operational conditions.

Both uneven distribution of the holes and less open area in the VD give a more even distribution of the simulated volatiles. Furthermore, the VD works better in the single bubble regime compared to the multiple bubble regime because the larger bubble movements and coalescence in the single bubble regime help the gas mixing inside the VD and the simulated volatile horizontal dispersion outside the VD. However, the bottom leakage may be higher when the volatile flow rate is high, when the open area of the distribution holes is small, or when the single bubble regime is applied. In the single bubble regime, the simulated volatiles detected at the lower level near the bottom opening of the VD are caused by both gas back mixing and bottom leakage. In the multiple bubble regime, there is no obvious bottom leakage found and the detected simulated volatiles at the lower level are caused by the gas back mixing.

AUTHOR INFORMATION

Corresponding Author

Xiaoyun Li − *Department of Space, Earth and Environment, Chalmers University of Technology, 412 96 Göteborg, Sweden;* orcid.org/0000-0002-8022-7998; Email: xiaoyun.li@chalmers.se

Authors

Anders Lyngfelt − *Department of Space, Earth and Environment, Chalmers University of Technology, 412 96 Göteborg, Sweden;* orcid.org/0000-0002-9561-6574

David Pallarès − *Department of Space, Earth and Environment, Chalmers University of Technology, 412 96 Göteborg, Sweden;* orcid.org/0000-0002-1574-4075

Carl Linderholm − *Department of Space, Earth and Environment, Chalmers University of Technology, 412 96 Göteborg, Sweden*

Tobias Mattisson − *Department of Space, Earth and Environment, Chalmers University of Technology, 412 96 Göteborg, Sweden;* orcid.org/0000-0003-3942-7434

Complete contact information is available at: https://pubs.acs.org/10.1021/acs.energyfuels.1c04159

Notes

The authors declare no competing financial interest.

ACKNOWLEDGMENTS

This work was funded by the Swedish Energy Agency (Project 46626-1).

NOMENCLATURE

Abbreviations

AD198 = air distributor with 198 holes
AD1660 = air distributor with 1660 holes
BECCS = bioenergy carbon capture and storage
bio-CLC = chemical looping combustion of biomass
CLC = chemical looping combustion
CLOU = chemical looping with oxygen uncoupling
FFT = fast Fourier transform
HSV = high-level sampled volatiles
LSV = low-level sampled volatiles
PSD = power spectral density
RSD = relative standard deviation
SD = standard deviation
VD = volatile distributor

Notations

A = open area of the orifices (m^2)
c_{cal} = ideal average CO_2 concentration in the cross section of the riser (ppm)
c_m = measured CO_2 concentration (ppm)
$c_{s,h_{1\to2}}$ = solids concentration in the middle of h_1 and h_2 (kg/m^3)
$c_{VD,mea}$ = CO_2 concentration measured inside VD (ppm)
$c_{VD,avg}$ = average CO_2 concentration inside VD (ppm)
$\overline{c}$ = average CO_2 ratio
c_H/c_L = ratio between the highest and lowest CO_2 concentration at HSV
C_d = orifice discharge coefficient
dp/dh = pressure drop gradient (kPa/m)
f_s = pressure sampling frequency (Hz)
Δf = frequency resolution (Hz)
$F(f)$ = Fourier transform of the autocorrelation sequence of the time series of pressure signals (kPa)
g = acceleration of gravity (m/s^2)
h_1 and h_2 = different heights of the pressure measurement positions (m)

https://doi.org/10.1021/acs.energyfuels.1c04159
Energy Fuels 2022, 36, 9571−9587

h_b = dense bed height inside the VD (m)
h_{bottom} = height of the bottom of the VD (m)
h_{hole} = height of the distribution holes (m)
Δh = distance between the dense bed height inside the VD and the distribution hole level (m)
L = number of pressure signal segments
MF_{CO_2} = CO_2 flow (m_n^3/h)
MF_{SA} = air flow used for simulating volatiles (m_n^3/h)
MF_{PA} = primary air flow for the main fluidization (m_n^3/h)
N_s = length of segments of the pressure signals
$P_{xx}(f)$ = power spectrum density (kPa^2/Hz)
$p_{windbox}$ = pressure inside the wind box (kPa)
p_0 = pressure at the bottom of the riser (kPa)
p_8 = pressure at the top of the riser (kPa)
Δp_{AD} = pressure drop over the air distributor (kPa)
Δp_{riser} = pressure drop along the riser (kPa)
p_{h_1} and p_{h_2} = pressures measured at height h_1 and h_2 (kPa)
p_{in} = pressure inside the VD measured at the top right corner (kPa)
p_{out} = pressure outside the VD measured at the back side of the riser at the distribution hole level (kPa)
$\overline{p}$ = average pressure (kPa)
u_0 = fluidization velocity (m/s)
u_{VD} and u_{VD}' = fluidization velocity inside the VD based on two calculation methods (m/s)
v = orifice velocity (m/s)
V_{ba} and V_{ba}' = bottom air flow from the main riser to the VD based on two calculation methods (m_n^3/h)
V_{CO_2} = CO_2 flow rate (m_n^3/h)
V_{pa} = primary air flow rate (m_n^3/h)
V_{sv} = simulated volatile flow rate (m_n^3/h)
$V_{orifice}$ = orifice gas flow (m_n^3/h)
$x_i(n)$ = time series of pressure signals (kPa)
ρ_{gas} = density of gas (air) (kg/m^3)
ρ_s = density of bed materials (kg/m^3)
σ = standard deviation of pressures (kPa)

REFERENCES

(1) Intergovernmental Panel on Climate Change (IPCC). 2021: Summary for Policymakers. In *Climate Change 2021: The Physical Science Basis. Contribution of Working Group I to the Sixth Assessment Report of the Intergovernmental Panel on Climate Change*; Masson-Delmotte, V., Zhai, P., Pirani, A., Connors, S. L., Péan, C., Berger, S., Caud, N., Chen, Y., Goldfarb, L., Gomis, M. I., Huang, M., Leitzell, K., Lonnoy, E., Matthews, J. B. R., Maycock, T. K., Waterfield, T., Yelekçi, O., Yu, R., Zhou, B., Eds.; Cambridge University Press: Cambridge, U.K., 2021; https://www.ipcc.ch/report/ar6/wg1/#top (accessed Dec 1, 2021).

(2) Lyngfelt, A. Chemical Looping Combustion: Status and Development Challenges. *Energy Fuels* **2020**, *34*, 9077−9093.

(3) Lyngfelt, A.; Brink, A.; Langørgen, Ø.; Mattisson, T.; Rydén, M.; Linderholm, C. 11,000 h of chemical-looping combustion operation—Where are we and where do we want to go? *Int. J. Greenhouse Gas Control* **2019**, *88*, 38−56.

(4) Abad, A.; Adánez, J.; Gayán, P.; de Diego, L. F.; García-Labiano, F.; Sprachmann, G. Conceptual design of a 100 MW_{th} CLC unit for solid fuel combustion. *Appl. Energy* **2015**, *157*, 462−474.

(5) Lyngfelt, A.; Leckner, B. A 1000 MW_{th} boiler for chemical-looping combustion of solid fuels—Discussion of design and costs. *Appl. Energy* **2015**, *157*, 475−487.

(6) Pallarès, D.; Johnsson, F. Macroscopic modelling of fluid dynamics in large-scale circulating fluidized beds. *Prog. Energy Combust. Sci.* **2006**, *32*, 539−569.

(7) Adánez-Rubio, I.; Abad, A.; Gayán, P.; de Diego, L. F.; García-Labiano, F.; Adánez, J. Biomass combustion with CO_2 capture by chemical looping with oxygen uncoupling (CLOU). *Fuel Process. Technol.* **2014**, *124*, 104−114.

(8) Mei, D.; Linderholm, C.; Lyngfelt, A. Performance of an oxy-polishing step in the 100 kW_{th} chemical looping combustion prototype. *Chem. Eng. J.* **2021**, *409*, 128202.

(9) Linderholm, C.; Lyngfelt, A.; Cuadrat, A.; Jerndal, E. Chemical-looping combustion of solid fuels—Operation in a 10 kW unit with two fuels, above-bed and in-bed fuel feed and two oxygen carriers, manganese ore and ilmenite. *Fuel* **2012**, *102*, 808−822.

(10) Pallarès, D.; Díez, P.; Johnsson, F. Experimental Analysis of Fuel Mixing Patterns in a Fluidized Bed. *Proceedings of the 12th International Conference on Fluidization—New Horizons in Fluidization Engineering*; Vancouver, British Columbia, Canada, May 13−17, 2007; https://dc.engconfintl.org/fluidization_xii/114.

(11) Köhler, A.; Pallarès, D.; Johnsson, F. Magnetic tracking of a fuel particle in a fluid-dynamically down-scaled fluidised bed. *Fuel Process. Technol.* **2017**, *162*, 147−156.

(12) Luo, H.; Lu, Z.; Jensen, P. A.; Glarborg, P.; Lin, W.; Dam-Johansen, K.; Wu, H. Experimental and modelling study on the influence of wood type, density, water content, and temperature on wood devolatilization. *Fuel* **2020**, *260*, 116410.

(13) Lyngfelt, A.; Linderholm, C. Chemical-Looping Combustion of Solid Fuels—Status and Recent Progress. *Energy Procedia* **2017**, *114*, 371−386.

(14) Schmitz, M.; Linderholm, C. J.; Lyngfelt, A. Chemical looping combustion of four different solid fuels using a manganese-silicon-titanium oxygen carrier. *Int. J. Greenhouse Gas Control* **2018**, *70*, 88−96.

(15) Mendiara, T.; Abad, A.; de Diego, L. F.; García-Labiano, F.; Gayán, P.; Adánez, J. Biomass combustion in a CLC system using an iron ore as an oxygen carrier. *Int. J. Greenhouse Gas Control* **2013**, *19*, 322−330.

(16) Ströhle, J.; Orth, M.; Epple, B. Chemical looping combustion of hard coal in a 1 MW_{th} pilot plant using ilmenite as oxygen carrier. *Appl. Energy* **2015**, *157*, 288−294.

(17) Berdugo Vilches, T.; Lind, F.; Rydén, M.; Thunman, H. Experience of more than 1000h of operation with oxygen carriers and solid biomass at large scale. *Appl. Energy* **2017**, *190*, 1174−1183.

(18) Lyngfelt, A.; Pallarés, D.; Linderholm, C.; Rydén, M.; Mattisson, T. Fördelare av gaser i fluidiserad bädd (Distributor of volatile gases in the bottom part of a fluidized bed). Swedish Patent Application 1400085-5, Feb 17, 2014.

(19) Gogolev, I.; Soleimanisalim, A. H.; Linderholm, C.; Lyngfelt, A. Commissioning, performance benchmarking, and investigation of alkali emissions in a 10 kW_{th} solid fuel chemical looping combustion pilot. *Fuel* **2021**, *287*, 119530.

(20) Li, X.; Lyngfelt, A.; Mattisson, T. An experimental study of a volatiles distributor for solid fuels chemical-looping combustion process. *Fuel Process. Technol.* **2021**, *220*, 106898.

(21) Shen, L.; Wu, J.; Xiao, J.; Song, Q.; Xiao, R. Chemical-Looping Combustion of Biomass in a 10 kW_{th} Reactor with Iron Oxide As an Oxygen Carrier. *Energy Fuels* **2009**, *23*, 2498−2505.

(22) Markström, P.; Linderholm, C.; Lyngfelt, A. Chemical-looping combustion of solid fuels—Design and operation of a 100 kW unit with bituminous coal. *Int. J. Greenhouse Gas Control* **2013**, *15*, 150−162.

(23) Linderholm, C.; Schmitz, M.; Knutsson, P.; Källén, M.; Lyngfelt, A. Use of Low-Volatile Solid Fuels in a 100 kW Chemical-Looping Combustor. *Energy Fuels* **2014**, *28*, 5942−5952.

(24) Linderholm, C.; Schmitz, M.; Knutsson, P.; Lyngfelt, A. Chemical-looping combustion in a 100-kW unit using a mixture of ilmenite and manganese ore as oxygen carrier. *Fuel* **2016**, *166*, 533−542.

(25) Svensson, A.; Johnsson, F.; Leckner, B. Bottom bed regimes in a circulating fluidized bed boiler. *Int. J. Multiphase Flow* **1996**, *22*, 1187−1204.

(26) Svensson, A.; Johnsson, F.; Leckner, B. Fluidization regimes in non-slugging fluidized beds: The influence of pressure drop across the air distributor. *Powder Technol.* **1996**, *86*, 299−312.

https://doi.org/10.1021/acs.energyfuels.1c04159
Energy Fuels 2022, 36, 9571−9587

(27) Karlsson, T.; Liu, X.; Pallarès, D.; Johnsson, F. Solids circulation in circulating fluidized beds with low riser aspect ratio and varying total solids inventory. *Powder Technol.* **2017**, *316*, 670−676.
(28) Djerf, T. Solids Flow in Large-Scale Circulating Fluidized Bed Furnaces. Ph.D. Thesis, Chalmers University of Technology, Göteborg, Sweden, 2021.
(29) Xiang, J.; Li, Q.; Tan, Z.; Zhang, Y. Characterization of the flow in a gas-solid bubbling fluidized bed by pressure fluctuation. *Chem. Eng. Sci.* **2017**, *174*, 93−103.
(30) Johnsson, F.; Zijerveld, R. C.; Schouten, J. C.; van den Bleek, C. M.; Leckner, B. Characterization of fluidization regimes by time-series analysis of pressure fluctuations. *Int. J. Multiphase Flow* **2000**, *26*, 663−715.
(31) Kunii, D.; Levenspiel, O. The Dense Bed: Distributors, Gas Jets, and Pumping Power. In *Fluidization Engineering*, 2nd ed.; Kunii, D., Levenspiel, O., Eds.; Butterworth-Heinemann: Boston, MA, 1991; Chapter 4, pp 95−113.
(32) *Cold Flow Model—Films of Volatiles' Distributor (VD)*; http://www.entek.chalmers.se/lyngfelt/co2/VDpaper2.html (accessed Dec 2021).
(33) Toomey, R. D.; Johnstone, H. F. Gaseous Fluidization of Solid Particles. *Chem. Eng. Prog.* **1952**, *48*, 220−226.
(34) Grace, J.; Clift, R. On the two-phase theory of fluidization. *Chem. Eng. Sci.* **1974**, *29*, 327−334.
(35) Kunii, D.; Levenspiel, O. Gas Dispersion and Gas Interchange in Bubbling Beds. In *Fluidization Engineering*, 2nd ed.; Kunii, D., Levenspiel, O., Eds.; Butterworth-Heinemann: Boston, MA, 1991; Chapter 10, pp 237−256.

https://doi.org/10.1021/acs.energyfuels.1c04159
Energy Fuels 2022, 36, 9571−9587